Journal of Power Sources 288 (2015) 473–481

Contents lists available at ScienceDirect

Journal of Power Sources

journal homepage: www.elsevier.com/locate/jpowsour

Investigating the effect of thermal gradients on stress in solid oxide fuel cell anodes using combined synchrotron radiation and thermal imaging

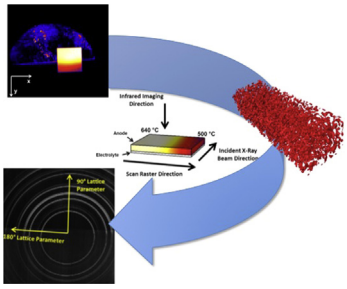
James B. Robinson [a], Leon D. Brown [a], Rhodri Jervis [a], Oluwadamilola O. Taiwo [a], Thomas M.M. Heenan [a], Jason Millichamp [a], Thomas J. Mason [a], Tobias P. Neville [a], Ralph Clague [b, c], David S. Eastwood [d, e], Christina Reinhard [f], Peter D. Lee [d, e], Daniel J.L. Brett [a], Paul R. Shearing [a, *]

[a] Electrochemical Innovation Lab, Department of Chemical Engineering, UCL, London WC1E 7JE, UK
[b] Intelligent Energy, Charnwood Building, Holywell Park, Ashbey Road, Loughborough, Leicestershire LE11 3GB, UK
[c] Energy Futures Lab, Imperial College London, South Kensington Campus, London SW7 2AZ, UK
[d] Research Complex at Harwell (RCaH), Rutherford Appleton Laboratory, Didcot, Oxfordshire OX11 0FA, UK
[e] School of Materials, University of Manchester, Oxford Road, Manchester M13 9PL, UK
[f] Diamond Light Source, Harwell Science and Innovation Campus, Didcot, Oxfordshire OX11 0DE, UK

HIGHLIGHTS

- Changes in lattice parameter in SOFC anode measured by novel technique.
- Thermal gradients cause non-uniform stress gradients in SOFC anodes.
- Changes in lattice parameters higher than expected from pure linear expansion.

GRAPHICAL ABSTRACT



ARTICLE INFO

Article history:
Received 14 January 2015
Received in revised form
26 March 2015
Accepted 16 April 2015

Keywords:
X-ray diffraction
Solid oxide fuel cell
Infrared imaging
Thermal imaging
Stress analysis
Synchrotron radiation

ABSTRACT

Thermal gradients can arise within solid oxide fuel cells (SOFCs) due to start-up and shut-down, non-uniform gas distribution, fast cycling and operation under internal reforming conditions. Here, the effects of operationally relevant thermal gradients on Ni/YSZ SOFC anode half cells are investigated using combined synchrotron X-ray diffraction and thermal imaging. The combination of these techniques has identified significant deviation from linear thermal expansion behaviour in a sample exposed to a one dimensional thermal gradient. Stress gradients are identified along isothermal regions due to the presence of a proximate thermal gradient, with tensile stress deviations of up to 75 MPa being observed across the sample at a constant temperature. Significant strain is also observed due to the presence of thermal gradients when compared to work carried out at isothermal conditions.

© 2015 The Authors. Published by Elsevier B.V. This is an open access article under the CC BY license (http://creativecommons.org/licenses/by/4.0/).

* Corresponding author.
E-mail address: p.shearing@ucl.ac.uk (P.R. Shearing).

http://dx.doi.org/10.1016/j.jpowsour.2015.04.104
0378-7753/© 2015 The Authors. Published by Elsevier B.V. This is an open access article under the CC BY license (http://creativecommons.org/licenses/by/4.0/).

Nomenclature

ε	strain
σ	stress
L	lattice parameter length
L_0	stress free lattice parameter length

1. Introduction

Solid oxide fuel cells (SOFCs) are considered to be a promising future power technology due to their high efficiency and fuel flexibility [1]; however, the widespread adoption of such devices has been inhibited by, amongst other things, the long term mechanical instability of the stack [2–5]. The cermet anode Ni-YSZ (yttria stabilised zirconia) is widely used in the construction of such cells with the intimate contact of metallic, ceramic and pore phases in the composite material providing a 3-dimensional distribution of triple phase boundaries (TPBs) in the electrode, maximising its electrochemical performance. However, the coefficient of thermal expansion (CTE) mismatch between the anode and electrolyte phase (often a thin YSZ layer) has been widely reported to be the main cause of thermomechanical failure of SOFCs [6,7].

Thermal imaging has previously been performed on pellet SOFCs by Brett et al. [8] who utilised the technique to evaluate heat transfer coefficients, and Pomfret et al. [9,10] who used a filtered CCD camera to investigate the carbon formation caused by employing methanol and ethanol as direct fuels for SOFCs. Additionally, Schöttl et al. [11] used thermal imaging to investigate the thermal gradients imposed by passing a cold gas stream onto an open cathode SOFC. However, to date, the difficulty in obtaining optical access has limited the use of thermal imaging on larger form factor SOFCs.

Thermal gradients in SOFCs are present due to a wide range of conditions, including thermal cycling to/from operating conditions [12], and under operation due to load following and localised electrochemical reactions [13]. These gradients can exacerbate degradation arising from the thermal expansion co-efficient mismatch between the metallic and ceramic phases [14]. The balance-of-plant is greatly increased by the need to minimise thermal gradients, reduce the prospect of thermally induced failure and prolong the stack lifetime. Finite element analysis (FEA) has indicated that thermal gradients of the order of 10^4 K m^{-1} may exist under internal reforming conditions [15] and that thermal gradients drastically increase the prospects of cell failure [16] by causing differential stress across the cell (indeed, these models also predict the presence of thermal gradients under steady state conditions [17–19]). Limited reports of experimental procedures investigating the effect of thermal gradients in operating SOFCs exist; however, it has been reported that large temperature gradients and localised hot spots are observed due to internal reforming on small form factor SOFCs [20,21].

Stresses in SOFCs arise due a range of conditions, including sintering during the manufacture of the cell and under operational conditions (caused by both thermal and physical effects) [22,23]. The mechanical failure of cells has been attributed to the compound nature of the cell construction, which results in in-plane stresses associated with CTE mismatch between the different layers being generated within the component layers. Indeed such stresses occur both macroscopically across the cell, and microscopically between the electrode and electrolyte layers, and within the anode, at the interface between the Ni and YSZ [13,24–26]. The Weibull distribution has been used by a number of authors to relate applied stress to the probabilistic failure behaviour of SOFC anodes under a range of conditions [16,27–29]. While the parameters used to characterise the Weibull distribution have been widely investigated [30,31] it has been shown that the Weibull parameters can be heavily dependent on the microstructure of the anode [32]. Analytical failure criteria for SOFCs have been described by Sanrantaridis and Atkinson [5], based upon work by Beuth [33], who also report that while macroscopic stress distributions in anode support cells may be low, local stresses can be result in internal damage particularly during redox cycling.

A wide range of FEA has been conducted upon SOFCs in order to predict the effects of cell treatment (i.e. redox cycling) and operation. Lin et al. [24] investigated the effect of stacking SOFCs, concluding that the CTE mismatch between seals and interconnects impacted significantly on the stresses experienced by the cells. In addition, the modelling indicated that thermal gradients were unavoidable due to the nature of operation of the cell. It has also been reported that the layer which experiences the most significant tensile stresses is the anode [13] both due to the thickness of this layer within the commonly used anode supported type cell and the significantly larger CTE mismatch across the Ni/YSZ interface than the cathode/electrolyte interface. Celik et al. [34] utilised FEA analysis to investigate the degradation of SOFCs at relevant operating temperatures; the authors conclude that stress can be decreased by increasing the YSZ or Ni content and the porosity of the anode; however, this results in reduced mechanical strength in the sample [35,36]. Celik et al. postulate that this enhanced effect of stress reduction due to the higher porosity is a result of stress relaxation through pores without restriction.

To date, a limited number of experiments utilising synchrotron X-ray diffraction (XRD) to explore operationally relevant SOFCs have been reported. A number of authors have utilised X-ray sources to identify residual stresses within SOFCs [37–42], while Sumi et al. [43] and Tanaka et al. [44] have also measured the effect of redox cycling on the internal stresses in anode supported Ni/ScSZ SOFCs. In addition to this, synchrotron radiation has been used to conduct high resolution tomography to analyse the internal microstructure of SOFC anodes [45–47]. Focused ion beam tomography has also been utilised in order to conduct microstructural stress analysis on SOFC anodes [48]; this work indicated that the stresses experienced by the Ni phase within the anode exceeded the yield strength, resulting in plastic deformation at temperatures approaching 800 °C. This highlights the need for fundamental studies in order to fully capture the effects of operationally relevant phenomena on SOFCs *in operando.*

To date, FEA modelling typically assumes bulk homogeneous mixtures of Ni and YSZ within the anode, as noted by Celik et al. [34]; however, in this work, the authors show experimentally that such an assumption may not be valid, resulting in inherent errors within modelling procedures. The results highlight the significant effect thermal gradients have upon both internal stresses and strains in SOFCs, while also showing the effects of a gradient located close to an isothermal region on the strain within the cell.

2. Experimental

All experiments were conducted using commercial anode supported half cells (AEB-27, Fuel Cell Materials, Ohio, USA) initially comprising a 220–260 μm NiO–YSZ anode layer and an electrolyte layer composed of 8-YSZ with a thickness of 6–10 μm. The cells were laser cut (Laser Micromachining Ltd., Denbighshire, United Kingdom) in order to produce tokens of 10 × 10 mm. Prior to the experiments the cells were reduced in a 10% H_2 in N_2 mixture for 3 h at 600 °C. Trace quantities (<3%) of NiO were observed in the reduced samples; however, the levels remained stable throughout

the duration of all experiments.

Experiments were performed at beamline I12 (JEEP) at Diamond Light Source using a bespoke furnace designed to generate thermal gradients across a sample [49]. The furnace consisting of two interlocking Inconel sections and a separate heating stage into which three individually controlled cartridge heaters (CIR-10121/240V, Omega Engineering Inc., Connecticut, USA) were placed, as seen in Fig. 1. The furnace contained three windows: two Kapton windows for the transmission of X-rays and a CaF_2 window to enable optical access for thermal imaging. The cell housing stage was bolted to the main beamline rotation stage in order to aid the coupling of the X-ray diffraction and thermal imaging. The temperature of the samples was adjusted at a maximum rate of 5 °C min^{-1} using the PID controlled heating stage and a hold time of between 10 and 15 min was applied before imaging in order to ensure any thermal oscillations were minimised. Forming gas (4% H_2 in N_2) was passed across the top of the sample at a rate of 80 mL min^{-1} through a heated line; this ensured the samples did not oxidise during the experiments and to reduce the duty on the cartridge heaters. Thermal gradients were obtained by positioning the SOFC sample across the edge of the heating stage; resulting in only part of the sample being heated (see Fig. 1). The magnitude of the gradient was tuned by careful adjustment of the portion of the sample in contact with the heating stage.

Thermal imaging was performed using an IR camera (FLIR SC5600MB, FLIR Systems France, Croissy–Beaubourg, France) which was calibrated for 15–250 °C and 250–1500 °C temperature ranges. These calibration settings were in turn modified, to a suitable range of expected temperatures for the given experiment, in order to obtain accurate thermal results. The combined transmittivity and emissivity of both the CaF_2 window and sample was accounted for prior to each scan by placing a thermocouple on the sample enabling an accurate calibration. The camera has an extended wavelength detector allowing detection of infrared light within the range 2.5 μm–7 μm. A 27 mm (F/3) lens was used throughout the imaging process, with the images recorded using commercially available software (FLIR ResearchIR, FLIR Systems, France). Due to the fixed working distance provided by the furnace, a pixel resolution of 74 μm was achieved for all infrared images. In order to limit the data storage requirements, images were recorded at 20 s intervals. To account for any PID controller oscillations, approximately 90 thermal images were averaged for each full, 30 min, scan of the sample. Thermal images were analysed using commercially available software (ResearchIR, FLIR ATS, France).

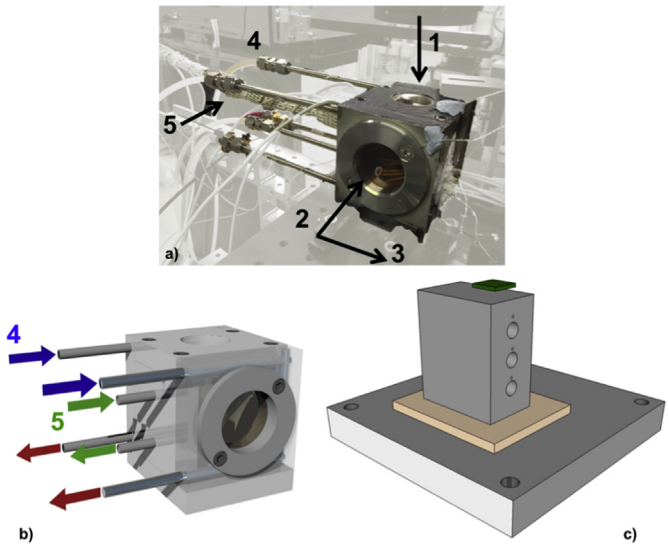


Fig. 1. Image (a) and drawing (b) of the furnace used in the experiment highlighting: (1) the infrared imaging direction; (2) the direction of the incident X-ray beam; and (3) the direction of stage translation during the experiment. The external lines indicated by 4 and 5 show the external cooling circuit and gas preheating lines respectively. Image (c) shows the furnace base complete with heating stage pyrophyllite insulating platform (brown) and sample (green). (For interpretation of the references to colour in this figure legend, the reader is referred to the web version of this article.)

Throughout the experiments a monochromatic X-ray beam with an energy of 80 keV was used. A Thales detector (Pixium RF4343, Thales Electron Devices S.A., France) consisting of a CsI scintillator on an amorphous Si substrate with a pixel size of 148 μm × 148 μm was utilised to collect the diffraction patterns. Coarse alignment of the samples was performed using X-ray imaging, followed by a second, finer, alignment via X-ray diffraction using a 20 μm square beam; this beam size was maintained throughout all experiments.

When suitable alignment was achieved, a calibration of the sample distance from the detector was performed using a CeO_2 standard. During the experiment, an exposure time of 80 s was used in order to obtain sufficient count levels to perform analysis of the sample. In total, diffraction data was collected horizontally along the anode – electrolyte interface at 20 discrete points equally spaced across the sample.

Le Bail fitting of the crystallographic data was performed using Topas (Bruker, Massachusetts, USA), to obtain both the in-plane (90°) and out-of-plane (180°) lattice parameter of the Ni face centred cubic unit cell.

Post-mortem focussed ion beam (FIB) tomography was carried out in order to characterise the Ni-YSZ structure. A Zeiss XB1540 FIB-SEM was used to collect the images, in all cases imaging was performed at 5 kV in SE2 mode to achieve suitable contrast between the pore and solid phases. All milling was conducted at 50 nA with Ga^+ ion beam accelerating voltages of 30 kV. The sample was pre-treated via gold sputtering to ensure sufficient electronic conductivity to achieve accurate SEM imaging. In total 76 sequential images were used for reconstruction enabling a reconstructed volume of 3250 μm^3. Reconstruction was performed using Avizo Fire (FEI, Oregon, USA) with post-mortem image analysis being conducted in Matlab (R2014a, Mathworks, Massachusetts, USA). Image analysis indicated a mean porosity of 18.7% through the reconstructed element.

3. Results and discussion

The nature of the experimental design of the furnace enabled simultaneous high resolution thermal imaging and X-ray diffraction; the use of thermal imaging also significantly simplifies and improves the measurement of thermal gradients which could not be measured easily using thermocouples. Fig. 2(a) shows a sample thermal image obtained at a furnace temperature of 640 °C, as measured by the control thermocouples. In addition, thermal gradients are shown in Fig. 2(b), these represent the average gradient observed throughout the length of the scan (typically 30 min in duration).

Fig. 2(a) shows a top down view of the sample, describing the x-y plane with a large thermal gradient clearly visible in one dimension along the y-axis of the sample; this corresponds to the scan raster direction. By contrast, isotherms are seen to run along the x-axis of the sample corresponding to the direction of the incident X-ray beam. Due to the thickness of the sample, it was assumed that there was no thermal gradient through the sample along the x-z plane. These isotherms enable accurate XRD analysis as all results were obtained in transmission by integrating the

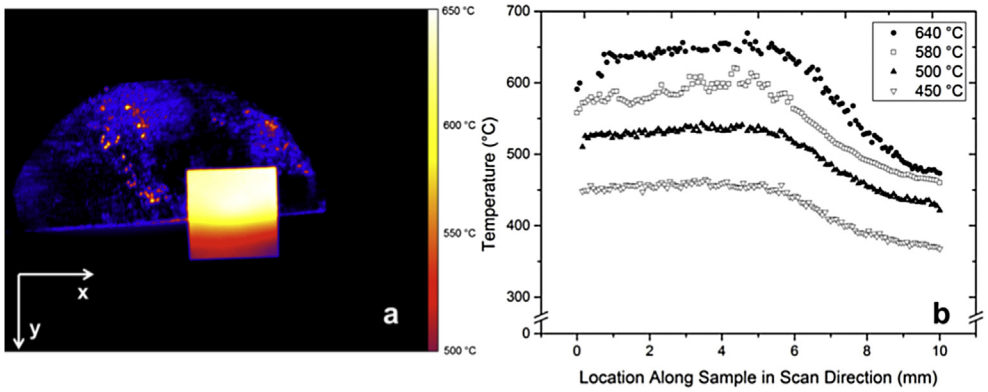


Fig. 2. (a) Sample infrared thermal image recorded at a furnace temperature of 640 °C; (b) Thermal gradients acquired from thermal imaging averaged across the length of the sample and the full duration of the scans for four nominal temperatures.

results throughout the thickness of the sample. The thermal gradients as seen in Fig. 2(b) correspond with thermal gradients of approximately 10^4 K m^{-1} which have been previously reported during internal reforming conditions in SOFCs [15].

Fig. 3 illustrates the sample showing both the anode and electrolyte which acts as a constraining layer due to the lower coefficient of thermal expansion [50] when compared to the anode layer. This constraint resulted in a slight bending of the sample towards the anode layer side within the colder region of the sample; a phenomena which was observed throughout all experiments.

Due to the geometry of the experimental setup the 90° and 180° Ni lattice parameters can be defined in accordance with the electrode/electrolyte interface. The 90° lattice parameter is seen to be vertically perpendicular to this interface (along the z-axis) with the 180° lattice parameter being parallel to the electrode/electrolyte interface (along with the y-axis). The thermal gradient is seen to be parallel to the 180° lattice parameter and thus the electrode/electrolyte interface. Due to these orientations the points analysed in the 90° direction are located along vertical isotherms, and thus unaffected by the presence of the thermal gradient. In contrast, the points analysed in the 180° direction, as defined in Fig. 3, are parallel to the thermal gradient; thus, are strongly affected by the gradient due to its orientation across the 50 μm X-ray beam.

Le Bail fitting was performed using Topas in order to obtain elemental analysis of the X-ray diffraction results with a sample fit shown for an 90° scan obtained from the centre of a sample at 625 °C in Fig. 4.

Fig. 4 shows the location of YSZ and Ni peaks obtained from the XRD patterns. The error trace also shown in Fig. 4 indicates that the location of the peaks in the fitted result correlates well with the expected results. In addition, the amplitude of the measured and fitted peaks differ by less than 5% in each case. Similar results were observed across the full length of the sample and at all temperatures observed for both the 90° and 180° cases. Trace quantities of NiO were observed during the fitting; however, the relative intensity of the measurements remained relatively constant throughout the 30 min scan in all cases, indicating no oxidation of the sample during the scans. The diffraction peaks in the 90° direction obtained at a range of temperatures from ambient to 600 °C are shown in Fig. 5.

Fig. 5 highlights the 90° Ni peaks obtained during Topas analysis over the range of temperatures examined during the experiment. It is evident that the location of the peaks shifts negatively with increased temperature with the Ni (022) peak shifting from a 2-theta angle of 7.22° to an angle of 7.17°. Additionally, it is evident

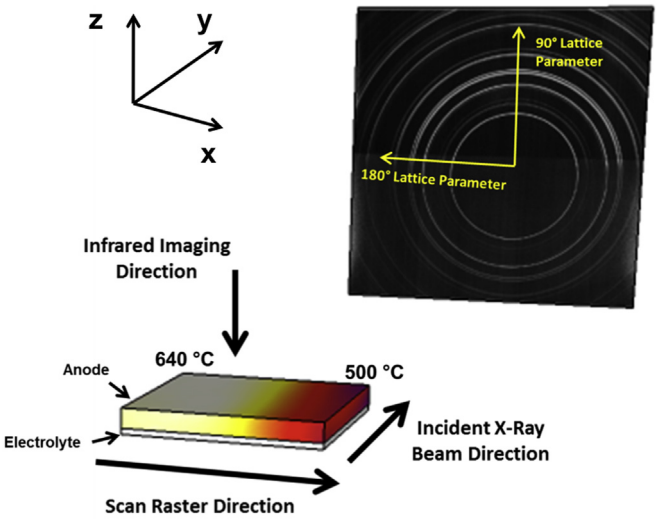


Fig. 3. Schematic of the Ni/YSZ half-cell indicating the direction of the incident X-ray beam, the scan raster direction, the imposed thermal gradient from 640 °C to 500 °C and the orientation of the infrared thermal imaging. Also shown is the direction of the 90° and 180° Ni lattice parameters which were used for all analysis.

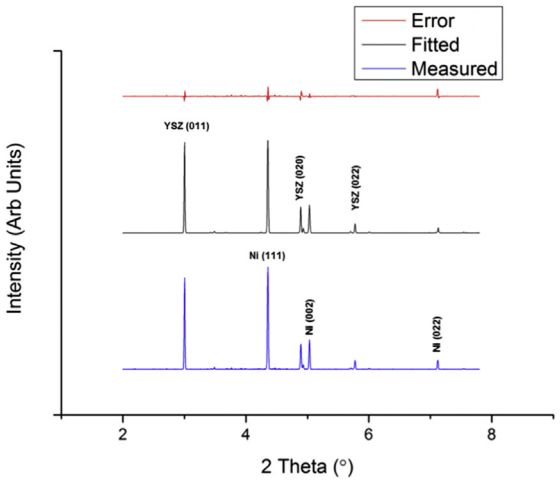


Fig. 4. Measured and fitted XRD diffraction patterns for a sample at 625 °C (located in the centre of the sample) up to a 2 theta angle of approximately 8° with the Ni and YSZ peaks highlighted in the measured and fitted patterns respectively. Also shown is the error trace of the fitting highlighting the fact that all peaks are fitted.

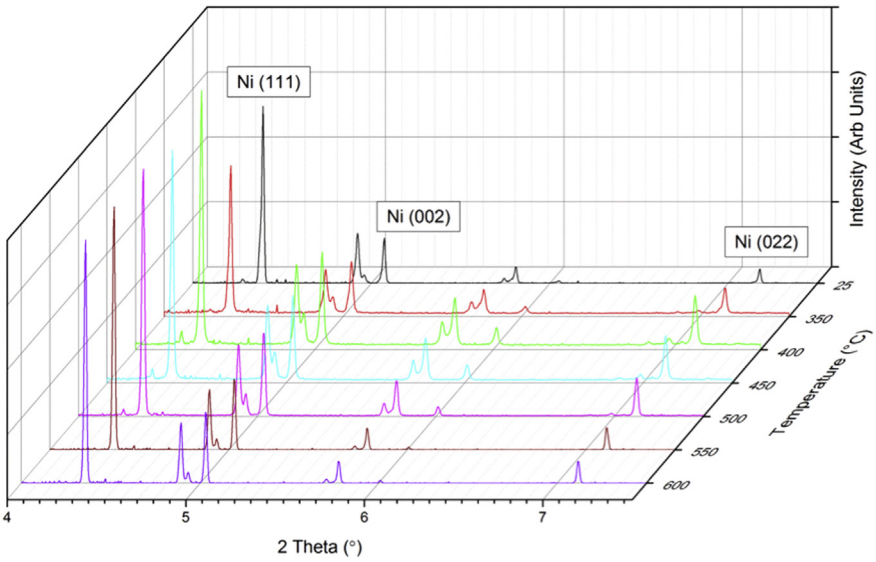


Fig. 5. X-ray diffraction patterns showing the change in location of Ni (highlighted) and YSZ peaks with increasing temperature from ambient (25 °C) to 600 °C. All XRD patterns shown are taken from the same scan location over the range of temperatures.

that the amplitude of the Ni peaks remains relatively stable, indicating a stable sample composition throughout the duration of the experiment; this enables direct comparison of the results obtained between temperatures. A small increase of NiO peaks is observed at a 2-theta angle of approximately 6.1° from 350 °C to 400 °C, with a subsequent reduction in the peaks from 400 °C to 600 °C.

As the Ni unit cell is face centred cubic, a pure Ni unit cell can be described by a single lattice parameter [51]; this, however, is not the case when the Ni is incorporated into a Ni/YSZ cermet, as seen in Fig. 6. The preparation of the anode involves the reduction of a NiO/YSZ layer to an active layer of Ni/YSZ, resulting in a volume change of up to 40% [52]. Because of the constraining effect of the YSZ electrolyte an offset between the 90° and 180° Ni lattice parameters occurs, as seen in Fig. 6. Due to the interconnected, complex 3-D structure of the Ni phase within the cermet, Ni grains will be randomly orientated throughout the mixture. Given this random orientation, defining a universal Poisson's ratio is not possible; rather, averaged Ni lattice parameter lengths in the 90° and 180° directions are described based on an assumption that the crystals are orientated with equal probability in all directions. These averaged parameters are obtained by calculating the eccentricity of the Ni diffraction signal integrated throughout the full 10 mm thickness of the sample.

The effect of incorporating Ni into the cermet mixture is highlighted in Fig. 6 which shows a constant offset between the averaged Ni 90° and 180° lattice parameters over a wide range of operationally relevant temperatures using data obtained at beamline I-12.

Fig. 6 highlights the elastic deformation caused by a uniform heating/cooling cycle which is displayed in both the averaged 90° and 180° lattice parameters under isothermal conditions. Stress relaxation was observed in an initial heating cycle (above 800 °C); however, in the subsequent heating/cooling cycles no relaxation was observed, indicating a single cycle was sufficient to relieve inherent strains within the sample. Once the inherent stresses had been relieved, a linear trend was observed in the Ni lattice parameters as the sample is uniformly heated from ambient, conforming to pure thermal expansion. When the sample is subsequently cooled from 950 °C to 400 °C the lattice parameters are seen to overlap, associated with elastic behaviour, with those obtained during the heating cycle, in this case corresponding with thermal contraction. In addition, the offset observed between the averaged 90° and 180° Ni lattice parameters is seen to be constant across the full range of temperatures. This constant offset indicates the thermal cycling impacts upon both the 90° and 180° averaged lattice parameters uniformly when under isothermal conditions. In

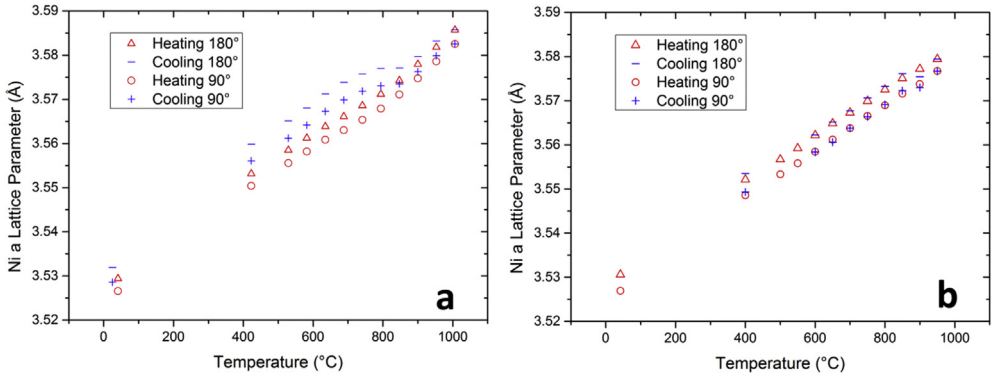


Fig. 6. Offset between Ni 90° and 180° lattice parameters due to the reduction of a NiO/YSZ layer to Ni/YSZ over a range of operationally relevant temperatures showing (a) stress relaxation in the sample during the first cycle and (b) subsequent cycles indicating strain relaxation had occurred within the relevant temperature ranges.

both the heating and cooling cycles shown in Fig. 6, the contribution to the change of Ni lattice parameter is a simple product of the temperature change and the coefficient of thermal expansion.

Fig. 7 shows the effects of thermal gradients on the averaged Ni 90° and 180° lattice parameters. The results are presented to show both the thermal gradient identified by thermal imaging and the lattice parameters obtained from XRD analysis.

The results displayed in Fig. 7 show a non-uniform contraction in the averaged 180° Ni lattice parameter with respect to the averaged 90° Ni lattice parameter. While the behaviour of the averaged 90° Ni lattice parameter is consistent with linear thermal contraction (there was no observed deviation from the expected close to plane stress condition as no thermal gradient exists in the 90° direction), the averaged Ni 180° lattice parameters show considerable deviation from the behaviour expected. Rather than a uniform offset between the two lattice parameters, as shown in Fig. 6, a convergence is evident along the length of the sample, coinciding with the onset of the thermal gradient. In addition, contraction of the averaged 180° lattice parameter is evident prior to the onset of the thermal gradient, indicating that the presence of a thermal gradient affects the lattice parameters, even in regions of constant temperature. This behaviour can be explained by a proposed 'nearest neighbour effect' (shown diagrammatically in Fig. 8), with the resultant contraction of the averaged 180° lattice parameters along the isothermal region (0–5 mm) being caused by the reduction in the Ni lattice parameter along the gradient. Given that the Ni must be interconnected throughout the anode to ensure sufficient electronic conductivity, a large contraction in the Ni unit cell in a single direction will increase the stress on its neighbouring unit cells resulting in exacerbated deformation as indicated in Fig. 7.

Fig. 8(a) shows the effect of discrete temperatures on the Ni/YSZ cermet which is constrained by a YSZ electrolyte layer due to the mismatch in CTE between the two component layers. Here, an offset between the 90° and 180° averaged lattice parameters is shown to be caused during the reduction process by the constraining electrolyte layer. However, due the uniform and discrete temperatures no interaction between thermally mismatched grains occurs and contraction occurs at equal rates for both lattice parameters. This contrasts with the effects observed in presence of a thermal gradient, as described by Fig. 8(b). Due to the thermal gradient, strains are manifested across interconnected grains at different temperatures and thus non-uniform levels of expansion occur. The effect of these interactions is to exacerbate contraction in the plane perpendicular to the constraining electrolyte layer (corresponding to the averaged 180° lattice parameter) and thus induce larger stresses upon the individual grains. In this instance the extent of deviation from a case of constant temperature will depend on the magnitude of the thermal gradient across the sample in all directions. Due to the nature of this experiment a one-dimensional thermal gradient was imposed resulting in deviations only in the averaged 180° lattice parameter (which is parallel to both the thermal gradient and the electrolyte layer). This effect will be influenced by the microstructure of the anode, with a high level of solid phase connectivity increasing the interaction between the grains. The microstructure of samples used throughout the study have been obtained using FIB tomography (see Fig. 9) with the mean porosity of the sample calculated to be 18.7%; additionally the connectivity of the pores was observed to be low indicating a high degree of solid phase connectivity.

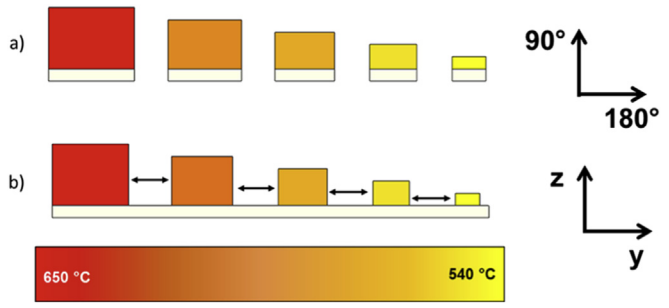


Fig. 8. Diagrammatic representation (not to scale) of the nearest neighbour effect. The effect of constraining a Ni/YSZ cermet (shown with a red to yellow colour scale) on a YSZ electrolyte (shown in white) for both (a) a number of discrete temperatures and (b) along a thermal gradient are described. (For interpretation of the references to colour in this figure legend, the reader is referred to the web version of this article.)

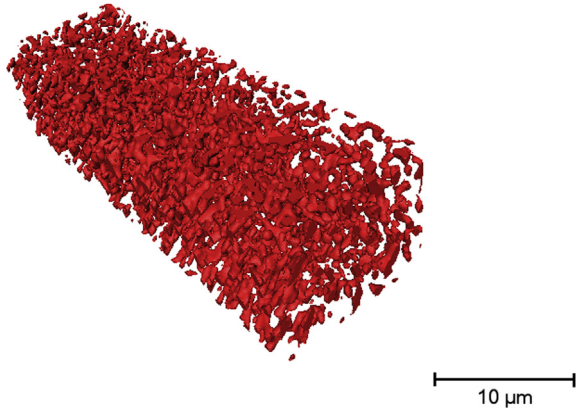


Fig. 9. Microstructural reconstruction of the pore phase within the Ni/YSZ anode obtained using FIB tomography.

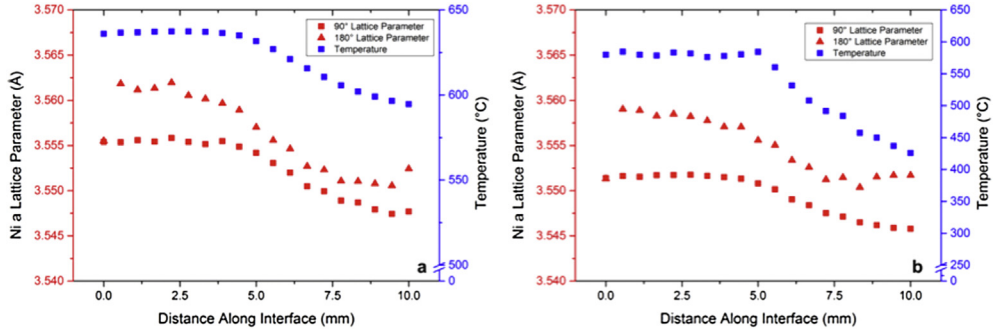


Fig. 7. Ni 90° and 180° lattice parameters (red) and the thermal gradient identified using infrared imaging (blue) measured across the length of the sample at two nominal temperatures; (a) 640 °C and (b) 590 °C. For reasons of readability the errors have been omitted from the plot; however, in the 90° and 180° directions the error is a maximum of 8.8×10^{-5} A and 1×10^{-3} A respectively with the average error along the thermal gradient being 4×10^{-4} in the 180° direction. The error in the temperature measurement is 1%. (For interpretation of the references to colour in this figure legend, the reader is referred to the web version of this article.)

The results of Fig. 6 were used as a control sample set in order to directly compare similar cells, both with and without a thermal gradient. In order to compare the two cases, models were developed using a linear fit in Matlab to relate the average lattice parameter length in both the 90° and 180° directions to the absolute temperature. Utilising this model and the thermal gradients observed in Fig. 7(a), an 'expected contraction' curve was generated. This curve enables a direct comparison between the extent of contraction in the averaged 180° Ni lattice parameter in the presence of a thermal gradient (Fig. 7(a)) with an expected contraction (obtained from a similar sample (Fig. 6)) investigated without the presence of a thermal gradient. Both the measured and modelled deviation from a normalised Ni 180° lattice parameter taken at 640 °C are displayed in Fig. 10. By comparing the expected and measured results it is evident that the presence of a thermal gradient causes a significantly amplified deviation in averaged 180° lattice parameter than would be expected from linear thermal expansion type behaviour. Once more, it is proposed that the 'nearest neighbour effect' results in significantly increased distortion in the Ni unit cell. The distortion shown above can be considered to be an indication of the stress experienced by the mean Ni unit cell in the 180° direction; while in the 90° direction linear thermal expansion behaviour is the only cause of thermal stress.

Thermal stress was calculated for points along the thermal gradient from the first principal definition of strain, which is given by

$$\varepsilon_{thermal} = \frac{L - L_0}{L_0} \quad (1)$$

where L is the Ni lattice parameter length at a given temperature and L_0 is the stress-free Ni lattice parameter length obtained at a sintering temperature of 1100 °C. The thermal stress then obtained at the discrete points along the thermal gradient by utilising the definition of Young's modulus for elastic materials to yield

$$\sigma_{thermal} = E \times \varepsilon_{thermal} \quad (2)$$

This calculation was performed using values of the Young's modulus obtained from Pihlatie et al. [53] at the relevant temperatures of interest. Fig. 11 shows the results of the calculated thermal stress as a function of temperature for the samples across three independent experiments.

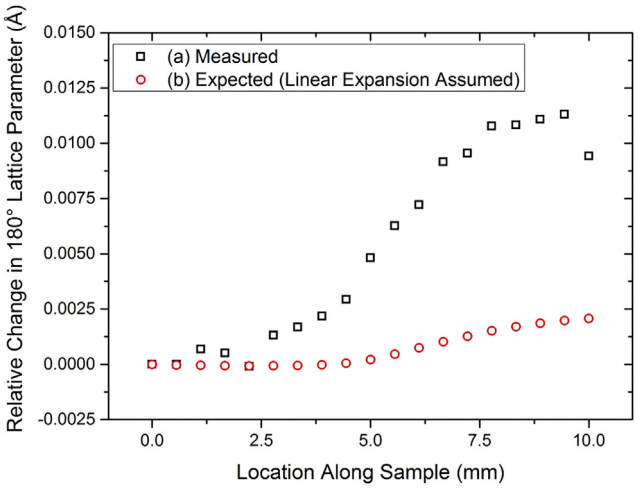


Fig. 10. Relative change of the measured Ni 180° lattice parameter and the Ni 180° lattice parameter which would be expected were pure linear thermal expansion assumed along the length of the sample using the data displayed in Fig. 6(a) at a furnace temperature of 640 °C.

Once more it is observed that non-thermal expansion type stress behaviour is displayed by the Ni 180° lattice parameter in Fig. 11. The linear behaviour displayed by the 90° lattice parameters, which result in a uniform grouping of lattice parameters obtained at constant temperatures, is consistent with behaviour expected along the isotherms in which the measurement was taken. In contrast, a stress gradient is observed along isotherms in the 180° lattice parameters. The magnitude of the isothermal stress is seen to range between 50 and 75 MPa in all cases which, when compared to the lowest absolute thermal stress along the isotherm, results in a stress gradient between 10 and 16% of the absolute tensile stress. This increased stress, along what is ostensibly a region where no thermally induced stress gradient is present, is significantly large under the externally unconstrained sample conditions in which the experiments were performed; however, by adding constraints to the edges of the sample, the stress within the sample will increase even further, thus increasing the chance of fracture of the sample.

4. Conclusions

Using synchrotron radiation, non-uniform thermal expansion has been observed in Ni/YSZ SOFC anode half cells due to the presence of operationally relevant thermal gradients. Analysis of the X-ray diffraction peaks shows a good fit for both the in and out of plane Ni lattice parameters for a simple face centred cubic unit cell, enabling analysis using commercial software which results in high accuracy correlation with the thermal gradients obtained. The thermal gradients, which were measured using infrared thermal imaging, have been shown to cause significant deviation from the behaviour expected if only linear thermal expansion type behaviour was considered.

Convergence between in and out of plane Ni lattice parameters, averaged through the thickness of the sample, is observed across the length of the sample coincident with the thermal gradient. The convergence is observed prior to the onset of the thermal gradient suggesting a 'nearest neighbour' effect which results from the connected nature of the Ni within the anode microstructure and results in deformation along isotherms due to the neighbouring unit cells contracting as a result of the thermal gradient.

Comparison with work performed on similar samples under isothermal conditions has demonstrated that significant deviations from the expected thermal expansion behaviour have been observed at operational temperatures indicating the presence of substantially higher strain in the Ni phase than would be expected.

Tensile stress has been observed within the Ni phase of the sample. It is observed that this tensile stress reduces with increasing temperature and behaves in a linear fashion for the 90° lattice parameters due to the experimental set-up. Thermal stress gradients of 10–15% of the absolute stress have been identified along isotherms for the averaged out of plane Ni lattice parameters caused by the presence of thermal gradients. Once more, such behaviour is explained by the 'nearest neighbour' theory. Additionally, constraining cells externally will increase this stress resulting in an increased likelihood of fracture of the cell.

Models must consider additional stresses when describing the stresses experienced within SOFC anodes during start-up and shut-down, heavy cycling or under internal reforming conditions which can cause large thermal gradients resulting in significant underestimation of the tensile stresses present.

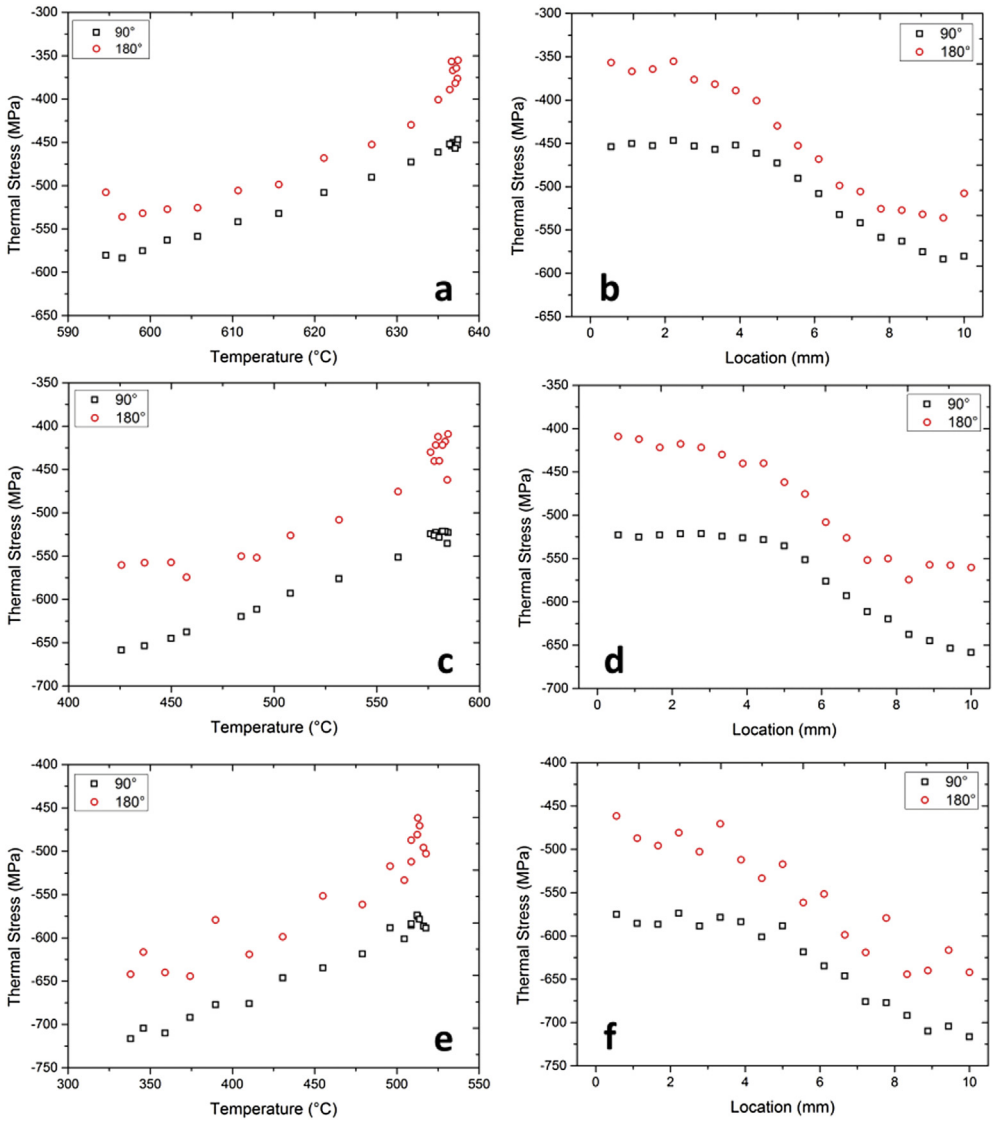


Fig. 11. The effect of thermal gradients upon the tensile stress within the sample with respect to the Ni lattice parameter lengths at a stress free temperature of 1100 °C for both the 90° and 180° Ni lattice parameters at nominal temperatures of: (a) 640 °C; (c) 590 °C; (e) 525 °C. Also shown is the location along the sample at which the stress is calculated at nominal temperatures of: (b) 640 °C; (d) 590 °C; (f) 525 °C.

Acknowledgements

The authors would like to acknowledge the EPSRC (EP/J001007/1) and the Royal Academy of Engineering for financial support. We thank Diamond Light Source for access to beamline I12 (EA8612-1) that contributed to the results presented here. The authors would also like to thank Mr. Samuel Cooper for his assistance at the beamline and Prof Alan Atkinson for useful discussion.

References

[1] R.M. Ormerod, Chem. Soc. Rev. 32 (2003) 17–28.
[2] H. Yokokawa, H. Tu, B. Iwanschitz, A. Mai, J. Power Sources 182 (2008) 400–412.
[3] W. Bujalski, C.M. Dikwal, K. Kendall, J. Power Sources 171 (2007) 96–100.
[4] D. Waldbillig, A. Wood, D.G. Ivey, J. Power Sources 145 (2005) 206–215.
[5] D. Sarantaridis, A. Atkinson, Fuel Cells 7 (2007) 246–258.
[6] W.Z. Zhu, S.C. Deevi, Mater. Sci. Eng. A 362 (2003) 228–239.
[7] S. Majumdar, T. Claar, B. Flandermeyer, J. Am. Ceram. Soc. 69 (1986) 628–633.
[8] D.J.L. Brett, P. Aguiar, R. Clague, A.J. Marquis, S. Schöttl, R. Simpson, N.P. Brandon, J. Power Sources 166 (2007) 112–119.
[9] M.B. Pomfret, D.A. Steinhurst, D.A. Kidwell, J.C. Owrutsky, J. Power Sources 195 (2010) 257–262.
[10] M.B. Pomfret, D.A. Steinhurst, J.C. Owrutsky, Energy & Fuels 25 (2011) 2633–2642.
[11] S. Scöttl, D.J.L. Brett, in: Engineering and Process Control Department Engineering and Process Control Department, National Physical Laboratory, 2006.
[12] H. Apfel, M. Rzepka, H. Tu, U. Stimming, J. Power Sources 154 (2006) 370–378.
[13] R. Clague, A.J. Marquis, N.P. Brandon, J. Power Sources 210 (2012) 224–232.
[14] C.-K. Lin, T.-T. Chen, Y.-P. Chyou, L.-K. Chiang, J. Power Sources 164 (2007) 238–251.
[15] H. Severson, M. Assadi, J. Fuel Cell Sci. Technol. 10 (2013) 061001.
[16] A. Nakajo, Z. Wuillemin, J. Van herle, D. Favrat, J. Power Sources 193 (2009) 203–215.
[17] P. Aguiar, C.S. Adjiman, N.P. Brandon, J. Power Sources 138 (2004) 120–136.
[18] E. Achenbach, J. Power Sources 49 (1994) 333–348.
[19] M.A. Khaleel, Z. Lin, P. Singh, W. Surdoval, D. Collin, J. Power Sources 130 (2004) 136–148.
[20] B. Morel, R. Roberge, S. Savoie, T.W. Napporn, M. Meunier, J. Power Sources 186 (2009) 89–95.
[21] P. Leone, A. Lanzini, B. Delhomme, G.A. Ortigoza-Villalba, F. Smeacetto, M. Santarelli, J. Power Sources 204 (2012) 100–105.
[22] C. Montross, H. Yokokawa, M. Dokiya, Br. Ceram. Trans. 101 (2002) 85–93.
[23] J. Malzbender, E. Wessel, R.W. Steinbrech, Solid State Ionics 176 (2005) 2201–2203.
[24] C.K. Lin, T.T. Chen, Y.P. Chyou, L.K. Chiang, J. Power Sources 164 (2007)

238–251.
[25] L. Liu, G.Y. Kim, A. Chandra, J. Power Sources 195 (2010) 2310–2318.
[26] A. Selimovic, M. Kemm, T. Torisson, M. Assadi, J. Power Sources 145 (2005) 463–469.
[27] T. Zhang, Q. Zhu, W.L. Huang, Z. Xie, X. Xin, J. Power Sources 182 (2008) 540–545.
[28] G. Anandakumar, N. Li, A. Verma, P. Singh, J.-H. Kim, J. Power Sources 195 (2010) 6659–6670.
[29] R. Clague, A.J. Marquis, N.P. Brandon, J. Power Sources 221 (2013) 290–299.
[30] M. Trunec, J. Eur. Ceram. Soc. 24 (2004) 645–651.
[31] A. Atkinson, A. Selçuk, Solid State Ionics 134 (2000) 59–66.
[32] H.L. Frandsen, T. Ramos, A. Faes, M. Pihlatie, K. Brodersen, J. Eur. Ceram. Soc. 32 (2012) 1041–1052.
[33] J.L. Beuth Jr., Int. J. Solids Struct. 29 (1992) 1657–1675.
[34] S. Celik, B. Ibrahimoglu, S. Toros, M.D. Mat, Int. J. Hydrogen Energy 39 (2014) 19119–19131.
[35] J.H. Yu, G.W. Park, S. Lee, S.K. Woo, J. Power Sources 163 (2007) 926–932.
[36] M. Radovic, E. Lara-Curzio, Acta Mater. 52 (2004) 5747–5756.
[37] J. Villanova, O. Sicardy, R. Fortunier, J.S. Micha, P. Bleuet, Nucl. Instrum. Methods B 268 (2010) 282–286.
[38] J. Villanova, C. Maurice, J.S. Micha, P. Bleuet, O. Sicardy, R. Fortunier, J. Appl. Crystallogr. 45 (2012) 926–935.
[39] H. Yakabe, Y. Baba, T. Sakurai, M. Satoh, I. Hirosawa, Y. Yoda, J. Power Sources 131 (2004) 278–284.
[40] W. Fischer, J. Malzbender, G. Blass, R.W. Steinbrech, J. Power Sources 150 (2005) 73–77.
[41] H. Yakabe, Y. Baba, T. Sakurai, Y. Yoshitaka, J. Power Sources 135 (2004) 9–16.
[42] J. Malzbender, W. Fischer, R.W. Steinbrech, J. Power Sources 182 (2008) 594–598.
[43] H. Sumi, K. Ukai, M. Yokoyama, Y. Mizutani, Y. Doi, S. Machiya, Y. Akiniwa, K. Tanaka, J. Fuel Cell Sci. Technol. 3 (2006) 68–74.
[44] K. Tanaka, Y. Akiniwa, H. Kimura, K. Ukai, M. Yokoyama, Y. Mizutani, Mater. Sci. Forum 571–572 (2008) 339–344.
[45] P.R. Shearing, R.S. Bradley, J. Gelb, S.N. Lee, A. Atkinson, P.J. Withers, N.P. Brandon, Electrochem. Solid St. 14 (2011) B117–B120.
[46] J. Villanova, P. Cloetens, H. Suhonen, J. Laurencin, F. Usseglio-Viretta, E. Lay, G. Delette, P. Bleuet, D. Jauffrès, D. Roussel, A. Lichtner, C. Martin, J. Mater. Sci. 49 (2014) 5626–5634.
[47] P.R. Shearing, J. Gelb, J. Yi, W.K. Lee, M. Drakopolous, N.P. Brandon, Electrochem. Commun. 12 (2010) 1021–1024.
[48] R. Clague, P.R. Shearing, P.D. Lee, Z. Zhang, D.J.L. Brett, A.J. Marquis, N.P. Brandon, J. Power Sources 196 (2011) 9018–9021.
[49] J.B. Robinson, L.D. Brown, R. Jervis, O.O. Taiwo, J. Millichamp, T.J. Mason, T.P. Neville, D.S. Eastwood, C. Reinhard, P.D. Lee, D.J.L. Brett, P.R. Shearing, J. Synchrotron Radiat. 21 (2014).
[50] F. Tietz, Ionics 5 (1999) 129–139.
[51] I.-K. Suh, H. Ohta, Y. Waseda, J. Mater. Sci. 23 (1988).
[52] P.R. Shearing, R.S. Bradley, J. Gelb, F. Tariq, P.J. Withers, N.P. Brandon, Solid State Ionics 216 (2012) 69–72.
[53] M. Pihlatie, A. Kaiser, M. Mogensen, J. Eur. Ceram. Soc. 29 (2009) 1657–1664.